LAWRENCE
LIVERMORE
NATIONAL
LABORATORY

LLNL-TR-464192

Broadband Infrared Heterodyne Spectrometer: Final Report

C. G. Stevens, C. T. Cunningham, J. W. Tringe

December 17, 2010

Disclaimer

This work performed under the auspices of the U.S. Department of Energy by Lawrence Livermore National Laboratory under Contract DE-AC52-07NA27344.

Broadband Infrared Heterodyne Spectrometer: Final Report

Charles Stevens, Chris Cunningham and Joe Tringe

Abstract

This report summarizes the most important results of our effort to develop a new class of infrared spectrometers based on a novel broadband heterodyne design. Our results indicate that this approach could lead to a near-room temperature operation with performance limited only by quantum noise carried by the incoming signal. Using a model quantum-well infrared photodetector (QWIP), we demonstrated key performance features of our approach. For example, we directly measured the beat frequency signal generated by superimposing local oscillator (LO) light of one frequency and signal light of another through a spectrograph, by injecting the LO light at a laterally displaced input location. In parallel with the development of this novel spectrometer, we modeled a new approach to reducing detector volume though plasmonic resonance effects. Since dark current scales directly with detector volume, this 'photon compression' can directly lead to lower currents. Our calculations indicate that dark current can be reduced by up to two orders of magnitude in an optimized 'superlens' structure. Taken together, our spectrometer and dark current reduction strategies provide a promising path toward room temperature operation of a mid-wave and possibly long-wave infrared spectrometer.

I. Heteryodyne spectrometer architecture and noise considerations

Hyper-spectral infrared instruments that are designed for extended stand-alone field use would benefit greatly by operating at or near ambient temperature without significantly sacrificing performance. The elimination of complex cryogenics that require additional power and thermal shielding reduces size, weight, power and cost. Estimates of the possible reduction in power requirements have been made and the pay-off can be substantial. One such estimate [1] is presented in Figure 1.

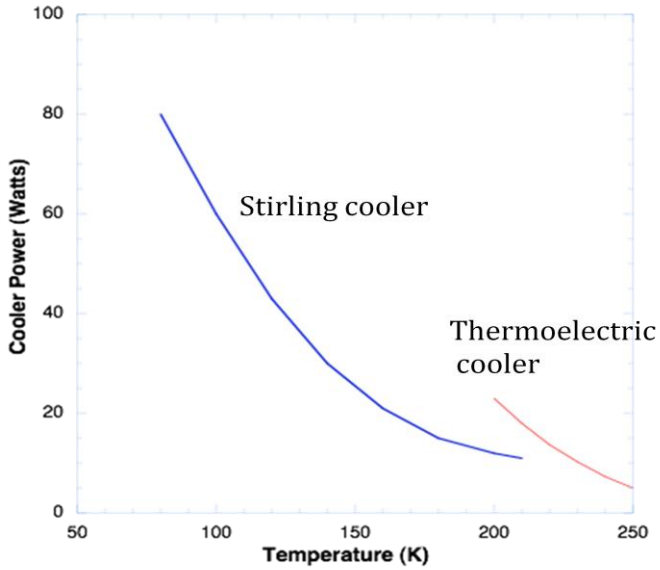

Figure 1. Cooler power vs. temperature for Stirling and thermoelectric technologies

Power consumption reductions of a factor of ~10 appear to be possible at operating temperature above 200K. Several approaches are being pursued, divided between thermal and photon

detectors. In thermal detection, absorbed radiation produces heat that in turn changes a measurable parameter of the system due to a rise in temperature. Commonly this is a change in electrical resistance. Thermal detectors can be uncooled and inexpensive, but have slow response and relatively low sensitivity. Photon detectors have much higher sensitivity but suffer from excessive dark current at elevated operating temperatures. Several approaches to reducing this current through different semi-conductor architectures have been proposed and implemented. Prominent among these the HOT (high operating temperature) non-equilibrium architecture [2,3] and the nBn (n-type, Blocking layer, n-type) architecture[4,5]. Despite significant progress, these approaches have not yet produced a detector with sufficiently suppressed dark current to allow operation of a hyperspectral instrument in the infrared at 200K or above.

A heterodyne approach provides an alternative with the potential for overcoming the dark current problem and approaching quantum-noise-limited performance. Our objective has been to explore the potential benefits of using the heterodyne approach for remote chemical sensing. Conventional heterodyne approaches use a sequential frequency scan to develop a spectrum. If the objective of the chemical sensing is to detect the presence of a chemical at low concentrations in the shortest possible time, the time taken to scan the spectrum becomes a problem. Conventional differential absorption lidar (DIAL) approaches avoid this problem though increased laser power, minimizing time spent dwelling on one spectral location.

With the advent of broadband infrared quantum cascade lasers [6], however, new capabilities for infrared spectrometry through heterodyning can now be considered. Here the radiant flux from a source such as a chemical plume is co-focused with a local laser onto an infrared detector, giving rise to a beat frequency in the GHz range. Frequency multiplexing becomes possible by injecting a broadband laser into a dispersive spectrometer at a physically displaced location that translates into a spectrally displaced image on a detector array. This is illustrated in Figure 2 below.

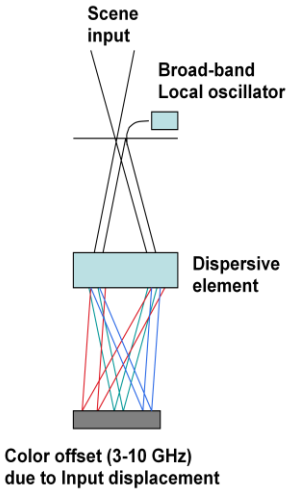

Figure 2. Broadband heterodyne spectrometer concept.

It can be shown that the photo-current generated by the signal (power P_{SIG}) and local oscillator (power P_{LO}) in a "square law" detector is

$$i = \frac{2e\eta}{h\nu}\left(P_{SIG}\cos^2\omega_{SIG}t + 2P_{SIG}^{1/2}P_{LO}^{1/2}\cos\omega_{SIG}t\cos\omega_{LO}t + P_{LO}\cos^2\omega_{LO}t\right)$$

or

$$i = \frac{2e\eta}{h\nu}\left[P_{SIG} + P_{LO} + 2P_{SIG}^{1/2}P_{LO}^{1/2}\cos((\omega_{LO} - \omega_{SIG})t\right]$$

where η, e and $h\nu$ are detection efficiency, electric charge and photon energy respectively. The first two terms give rise to a DC current, while the latter term is the intermediate frequency or "beat" frequency carrying the signal of interest. The expression for the signal to noise ratio of the current generated by the detector is given by

$$S/N = \frac{\frac{1}{2}\eta N_{SIG}^{1/2}N_{LO}^{1/2}}{\left[N_{SIG} + N_{LO} + N_{dark} + N_{back} + N_{other}\right]^{1/2}}$$

where we have converted power to total number of collected electrons over the integration time. A local oscillator with sufficient power can dominate the other terms in the denominator and the signal to noise ratio for the signal emerging from the detector becomes

USE the "½" symbol below

$$S/N = 1/2\eta N_{SIG}^{1/2}$$

in the quantum noise limit.

The efficiency term embodies several factors that are not normally encountered in a standard detection scheme. Along with the photo-detection efficiency, a linearly-polarized local oscillator will result in an additional factor of ½. Certain phase coherence between the signal and local oscillator must be established. The relative phase of each of the light waves and, therefore, the phase of the beat signal, must be constant over an area on the order of the size of the diffraction pattern of a point source. In other words, the product of the solid angular spread times the detector area should be about the area of the square of the wavelength, or $\Omega A \sim \lambda^2$. Incorporating these factors and assuming an efficiency factor of 0.5, the expected signal to noise ratio for a 90 % emissive gray body source at 300K as a function of wavelength is shown in Figure 3. The bandwidth (B) of the system is set at 0.1cm^{-1} and the integration time(t) is 1 sec. The ratio scales as $(Bt)^{1/2}$. This is a favorable upper limit in that it assumes good optical mode matching, good detector quantum efficiency and noise-free photoelectron capture.

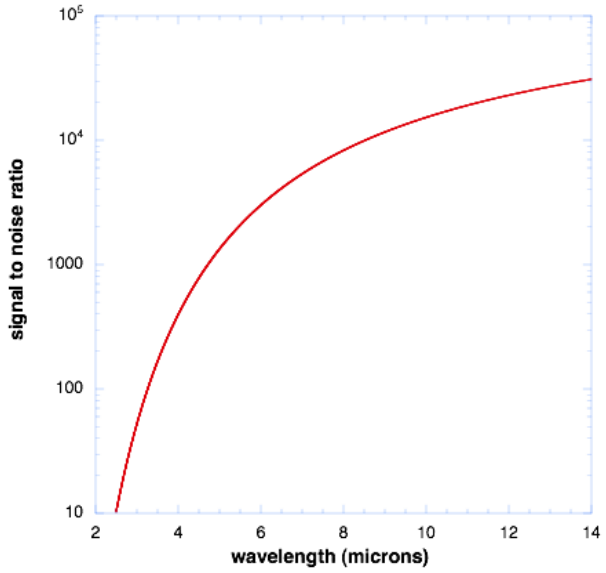

Figure 3. Signal-to-noise ratio for a 90 % emissive gray body source at 300K as a function of wavelength for a heterodyne detector, assuming an efficiency factor of 0.5.

II. Quantum well infrared photodetector (QWIP)

To demonstrate the potential of heterodyne for remote chemical sensing, we employed a "square-law" quantum well infrared photodetector (QWIP) with high frequency response covering the ~5 GHz spectral resolution of the spectrum analyzer, an echelle grating spectrograph. In general, quantum well detectors can have very high frequency response. These multi-layer semiconductor structures are routinely fabricated with atomic-layer control by molecular beam epitaxy. Common structures are built as inter-subband transition devices where the electronic transition occurs between states confined in quantum wells. The quantum wells are created by using alternating layers of a small bandgap material (absorbing layer) and a large bandgap material (barrier). The width of the absorbing layer determines the wavelength range of the detector with a number of layers required for absorption efficiency. In the mid-infrared region QWIPs are based on a GaAs substrate with InGaAs as the absorber and InAlAs as the barrier. Varying amounts of In and Al are used to tailor wavelength and barrier properties. Adjusting the Al mole fraction in the barrier layers can precisely control the height of the potential barrier.

For our heterodyne experiments, we required that the detector have a good response at high frequencies (tens of GHz). To create infrared detectors which satisfied this requirement, we partnered with the group led by Dr. Sarath Gunapala at JPL. The Gunapala group has been a leader in the development of these detectors, and they can readily fabricate small QWIP arrays.

Our design target wavelength range is in the mid-infrared, where high-efficiency quantum cascade lasers are just emerging from research laboratories.[7] QWIPs were fabricated at JPL using alternating layers of $In_{.1}Ga_{.9}$ As and $In_{.74}Al_{.26}As$; the former was used as absorber layer and the latter as a barrier. The spectral response of this device covers the region from ~3 μm to 4.5 μm. The detector contains 100 quantum wells, each 35 nm in width. The intersubband absorptivity is 1520 cm^{-1}, yielding an expected overall peak absorption efficiency of 40%.

A scanning electron microscope image of the detector is shown in Figure 4. The 20 µm detector is connected to a planar V-band waveguide by a small bridge. The planar waveguide is wire bonded to an SMA connector/cable. This design, as discussed later, should provide frequency response up to ~20 GHz.

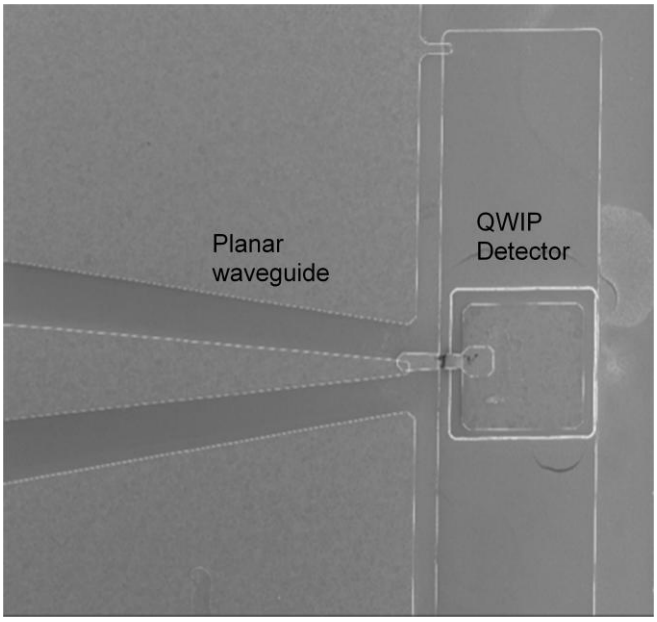

Figure 4. QWIP photodetector with planar waveguide for high-frequency response

For our experiments at LLNL, this detector was biased using a bias-tee (Wiltron K250). QWIP detectors operating in photoconductive mode can have dark currents that are considerably higher than found in HgCdTe. We measured the dark current of our detector as a function of bias voltage and temperature using a Keithley 6487 picoammeter. The results are shown in Figure 5.

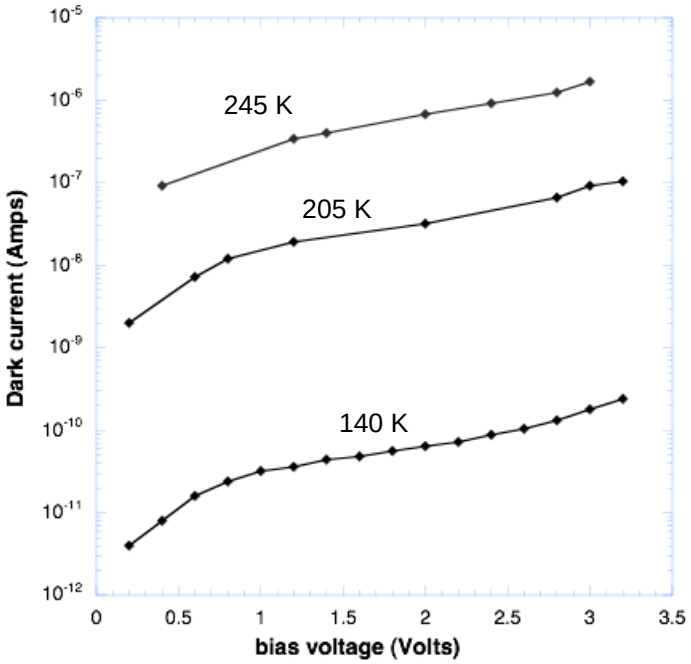

Figure 5. Dark current as a function of bias voltage for a QWIP used for heterodyne experiments, for temperatures 140, 205 and 245 K.

III. Heterodyne experiments

The object of these experiments was to test the concept that heterodyne signals can be generated by superimposing local oscillator (LO) light of one frequency and signal light of another through a spectrograph by injecting the LO light at an input location that is laterally displaced relative to the input location of the signal light. This physical displacement translates into a spectral displacement after grating dispersion when each detector pixel intercepts two wavelength bands. The spectrograph used for these experiments was custom-designed and fabricated at LLNL.[8] The spectrometer is a cross-dispersion echelle design with an f/10 entrance collection optic, a 23 groove/mm echelle grating oriented in Littrow mode and an f/3.5 condensing optic. The nominal dispersion and resolving power in the region of the infrared HeNe laser wavelength (3.39 μm) are 0.004 cm^{-1}/μm and 1.2×10^5, respectively. The 20 μm pixel size should intercept a spectral bin of~ 0.1 cm^{-1}.

The spectrometer is coupled to the light sources through ZrF_2 fibers having 50 μm core diameters. Ideally, the image of the entrance fiber is condensed to ~18 μm in the focal plane, just matching the QWIP pixel. The actual spot size depends on the effects of spectrometer aberration. We measured the actual spot size using the 3.39 μm wavelength from the infrared HeNe laser. A 5 μm pinhole located at the focal plane of the spectrometer was scanned in front of a HgCdTe detector. The results, presented in Figure 6, reveal a focal spot with a full-width at half maximum (FWHM) of ~ 25 μm, close to the aberration-free limit. Most of the laser light, ~87%, should be captured by a 20 μm pixel.

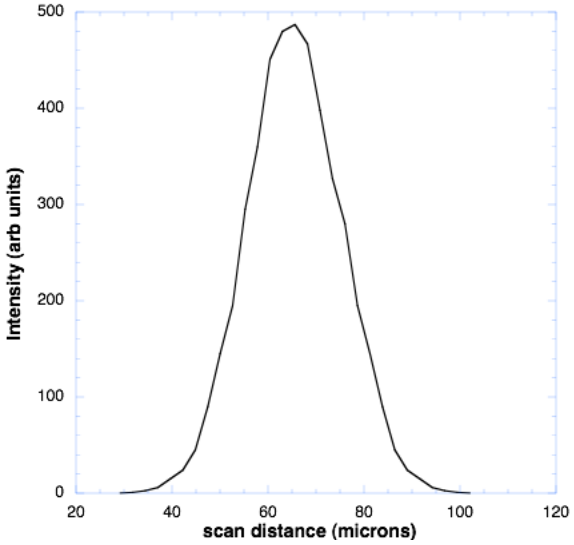

Figure 6. Detector signal as a function of scan distance for ZrF_2 fibers having 50 µm core diameters, indicating a focal spot with a FWHM of ~ 25 µm.

For heterodyne efficiency we want the product of the optical solid angle times the detector area to be ~ λ^2. The spectrometer detection etendue at 5×10^{-7} cm^2 steradians is ~ 5 times the ideal at 3.39 µm. This will degrade the heterodyne efficiency by the square root of that factor, ~ 2 times.

The heterodyne experiments were conducted using two configurations: a standard heterodyne setup and a configuration that passed light through the spectrometer. The standard heterodyne setup used the 3.39 µm HeNe laser as the local oscillator and a blackbody source as signal. The laser beam diameter was enlarged with a beam expander, combined with the signal source using a 50/50 beam splitter, and focused onto the QWIP detector with an F/2 lens.

The spectrometer experiments employed two optical configurations. In the first, the local oscillator and the signal source were combined and focused with an F/10 lens onto a single fiber that couples the light into the spectrometer. This sets a calibration standard for the heterodyne efficiency through the spectrometer. In the second configuration, shown in Figure 7, a fiber assembly was employed with separated fibers at the input end and a close-coupled lateral array at the spectrometer entrance. The 100 µm center-to-center spacing at the entrance translates into a 4 GHz offset in the detector plane.

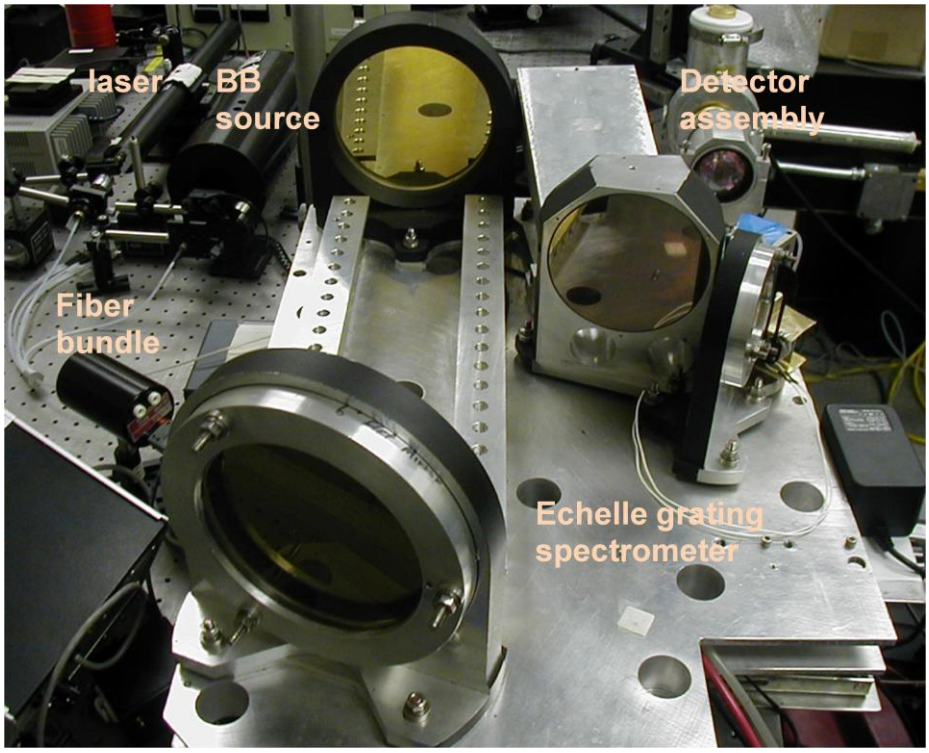

Figure 7. Experimental design for heterodyne spectrometer experiments.

The detector was followed by a 4 GHz amplifier (MITEQ AFS3), a rectifying Schottky diode (SMS392) and a lock-in amplifier (SRS510). The black body signal source is modulated with a synchronous mechanical chopper and the temperature adjusted to approximately 60 C, emulating a 30% sunlight reflective surface as discussed earlier. The results for the standard beam-splitter arrangement and the through-spectrometer arrangement are shown in Figure 8. The beamsplitter configuration result is indicated by the red triangle and the spectrometer results by blue ones. The points are located at the center of the beat frequency range for each experiment. The beamsplitter signal level is higher than the spectrometer signal presumably due to the sampling of frequencies to either side of the local oscillator frequency. The solid line is the response fall-off of the 4 GHz amplifier, scaled to coincide with the direct overlap experimental value. The signal level for the beam splitter and direct overlap are 1% and 0.4% of the theoretical maximum respectively. A significant fraction of this is due to the ~8% quantum efficiency of the detector, considerably smaller than the maximum 40% which has been demonstrated in optimized devices. The reason for this is unclear. Another loss factor of 0.25 is expected from the linear polarization of the laser and the 50% duty factor of the signal chopper. The remaining loss factor of 0.3 can be

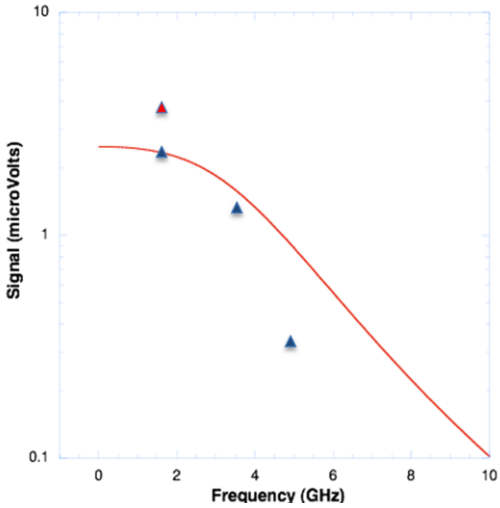

Figure 8. Signal as a function of frequency with the beam-splitter, through-spectrometer configuration. The solid line indicates the signal cut-off expected based on known amplifier.

attributed to fiber coupling, spectrometer throughput and beam mode matching (including beam splitter efficiency in that configuration). The signal generated by the overlap of adjacent fibers shows an expected roll-off (within noise) due to the 3dB roll-off expected at 4 GHz. The signal generated by a fiber once removed shows significantly more roll-off than can be attributed to the amplifier. The roll-off frequency is determined first by the carrier lifetime-limited response frequency and should be near 30 GHz. [9]. The detection circuit can be modeled as a current source through a circuit having a parasitic inductance is series with a 50 ohm amplifier input resistance, and in parallel with the detector capacitance. The impedance for this circuit is given by

$$Z(\omega) = \left| \frac{R + i\omega L}{1 + i\omega C \cdot (R + i\omega L)} \right|$$

The intrinsic capacitance of the detector (~0.1pF) and the inductance due to the wire bonds connecting the detector to the waveguide/ SMA transmission line (~ 1 nH) should lead to a 3 dB roll-off at ~ 25 GHz. The origin of the experimentally-observed roll-off at 4 GHz is therefore not known.

IV. Discussion and Conclusions

Despite using a single laser source as local oscillator, these experiments demonstrate the basic operating principle of a potentially multiplexing, broadband heterodyne approach. The single frequency laser can be replaced by a broadband laser source, and dispersed through the spectrometer. The development of broadband quantum cascade infrared lasers, first reported in 2002 by a Bell Laboratory group [10], offers a potential for robust local oscillator option required to implement this approach. The 5 mW local oscillator used here provided sufficient power to exceed the noise sources with the detector operating at 245 K. The LO generated ~ 1e14 photo-electrons/sec against a dark current of 6e12 e-/sec an estimated Johnson noise at 1e12e-/sec and background level of less than 1000 e-/sec over the 3-4 μm band.

Given the performance of state-of-the art detectors, a LO minimum power requirement can be established. A survey of the literature for detector performance has yielded the available detectivity (D* in units of cm $Hz^{1/2}$/Watt) values for a wide variety of detector technologies. The results at an operating temperature of 200K for a range of cut-off wavelengths and detector types are presented in Figure 9. The temperature of 200K is the highest temperature that included all the detector types and is probably the lowest desirable temperature target for present purposes. The red points are examples of different HgCdTe detector technologies. The conventional VIGO detector[11] has a frequency roll-off at ~ 1 GHz. The DRS HOT detector[1] and the Qinetic (nBn) detector[2] have intrinsically low frequency response and are shown for comparison.

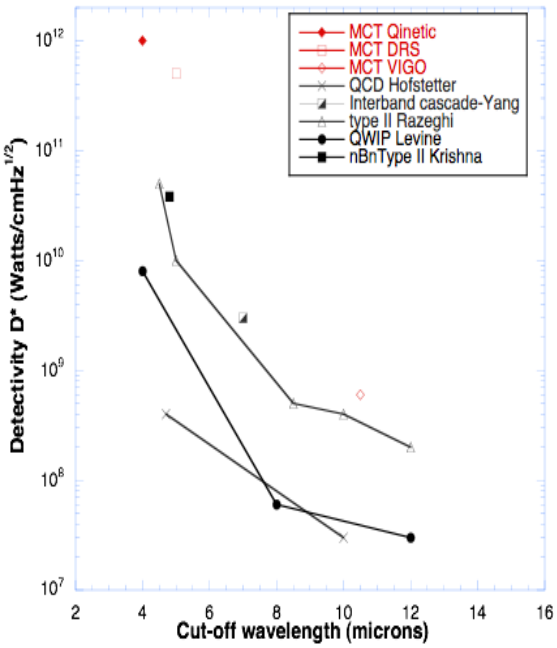

Figure 9. Detectivity as a function of wavelength for various state-of-the-art detector technologies.

The normalized dark current (A/cm^2) is related to the detectivity by the relation

$$J_{dark} = \frac{\frac{1}{2}\eta q}{(D^* h\nu)^2}$$

The local oscillator power is then related to J_{dark} as

$$P_{LO} >> \frac{h\upsilon}{q}\left(\frac{J_{dark}}{\eta}\right)A$$

where $h\nu$ and q assume their familiar roles, η is the detector quantum efficiency and A is the detector area. Assuming a cutoff frequency of 4 μm with a detectivity of 6e+10 and a quantum efficiency of 40%, a power requirement of > 0.01 μWatts is implied. The Johnson noise level can impose a further requirement for LO power and depends on the resistance in the detection circuit. If we assume a minimum of 50 Ω for high speed detection, we find a power requirement of > 0.1 μW.

The Gmachl group has demonstrated a 4–5μm continuous wave (cw) quantum cascade laser (QCL) operating at 285K with 1 W output and 5% wall plug efficiency. [12] Adjusting the Gmachl group (results ??), laser power levels consume only 1 W total over the 400 cm^{-1} span, and provide ~ 12.5 μW per cm^{-1} interval, considerably more than the required power level. This power would be sufficient for more than 50 spatial images. While not yet experimentally demonstrated, adjusting the well width of the QCL would provide a LO in the more important 3 to 4 micron spectral region.

Implementing the broadband heterodyne concept in the mid-infrared spectral region has some limitations. The photon flux in a 3 GHz bandwidth at the λ^2 etendue limit is low (~ $3x10^4$/sec). Molecules of interest in this spectral region have absorption coefficients that are in the neighborhood of 10^{-3}, e.g. HCl, dodecane. Consequently, at the shot noise limit, a detection threshold target of 1 ppm.m requires ~ 100 seconds of integration time. This would be reduced to ~ 30 seconds by increasing the bandwidth to 30 GHz (1 cm^{-1}).

Moving to the longwave spectral region we find a significant increase in the photon flux, but concomitantly an increase the detector dark current. Consider now the LO requirements for operating at 10 μm with a 12 μm cutoff wavelength. A detectivity of 3e+8 is assumed along with a 40 μm detector size. The required LO power is then greater than 4 mW/pixel.

Broad continuum lasers in the long-wave IR region have been under continuous development since the original Cappasso report. Among the most promising are the works of the Gmachl group at Princeton [13] and the Faist group at Neuchatel, Switzerland.[14] Significant improvement in wall-plug efficiency at room temperature (~20%) have also been accomplished by the Razeghi group at Northwestern University.[15] The Gmachl group has fabricated a 7-9μm laser generating 1 W of peak power at 4% efficiency, and the Faist group has fabricated an 8.2-10.4 μm laser capable of over 1 W of peak power at 6.25% efficiency. These pulsed lasers both operate at room temperature, with duty factor 5%. The relatively large photon flux in the long-wave region (~ 1e+8/sec) means we can sacrifice signal photons and still achieve significant S/N performance.

Assuming that no further developments take place in approaching cw operation, the 5% duty factor represents a drop in S/N from ~ 1e+4 to 2e+3 for a 1 second observation and 3 GHz bandwidth. The target power requirement range is less than10 Watts. Assuming a LO power requirement of 20 mWatts for good heterodyne performance, and a 10 Watt power consumption at 5% efficiency, we have enough LO power for 25 spectral bins at 3 GHz or only 2.5 cm^{-1}. A QWIP detector can function with reasonable efficiency up to 50 GHz or so with a carefully designed circuit.[9] Operating at 30GHz per bin stretches the coverage to 25 cm^{-1}. A desirable target for spectral coverage would, however, be at least 250 cm^{-1}.

One approach to reducing the power requirements involves reducing the volume of the detector. The above estimates for power are based on an F/3 condensing lens. A tenfold decrease in power can be realized through an F/1 lens. Alternatively, a factor of 16 in dark current reduction has been achieved by VIGO for MCT detectors in the long-wave region through the use of high index immersion lens technology.[16]

Another approach with potentially even larger payoff involves the use of plasmonic lenses, where reduction both in detector area and depth is possible. This can lead to power reductions of a hundred-fold or more, as discussed in Section V.

V. Introduction to dark-current reduction: power flow to a small HgCdTe detector in a conical cavity

The dark current in a semiconducting detector is proportional to the product of the rate of production of charge carriers per unit volume (a function of temperature) times the detector volume. Thus, noise can be reduced by making the detector smaller as well as cooler, and cooling requirements will also improve. A telescope can be used to focus the incident light, but

diffraction limits the size of the focus in an extended medium to the order of the wavelength and the detector must have sufficient optical depth to absorb the radiation.

Creating the focus in a refractive medium would be advantageous, since the local wavelength there could be a few times smaller than that in air; an order-of-magnitude reduction in the detector cross-section might be gained.

An elaboration of this notion is to channel the radiation in a waveguide filled with refractive material to a small cross section before it encounters the detector. A conical waveguide is straightforward to analyze, and furthermore (unlike a cylindrical waveguide) does not exhibit a cut-off frequency limiting the size of the propagating wave. Practical issues arise, however, where the waveguide diameter becomes smaller than a half wavelength in the bulk material, but this is still much smaller than a diffraction-limited focus. The extent of the detector along the cone axis can also be smaller than unit optical depth in the bulk medium, and the taper of the cone further reduces the detector size.

We begin our treatment of this concept in Section VI with the derivation of the normal modes of the electromagnetic fields in a conducting cone. (This treatment is presented first since understanding the behavior of the lowest-order mode is fundamental to further quantitative discussion.) The modes can be expressed analytically in terms of Bessel and Legendre functions. We base our discussion on Jackson's treatment of cylindrical waveguides and fibers, which we extend to a conical geometry. This shows that the field cannot be free of an axial component; the coefficient of this component satisfies the scalar wave equation; and from it the remainder of the field can be determined.[17]

In Section VII we present an initial effectiveness analysis of the concept. First, we present some simple rules-of-thumb that indicate that the ratio of power to volume (P/V) in the conical detector should be roughly two orders of magnitude greater than for a conventional cylindrical detector of similar diameter. For a more detailed treatment we consider the electromagnetic fields in the cone and detector explicitly to evaluate the net transmission of power into the detector, and we optimize certain parameters for maximum power-to-volume. Results are presented for notional point design parameters for a HgCdTe photodiode with Cd concentrations for operation between 4.6 and 6μ. The conical detector has P/V more than 200 times greater than the conventional detector.

In Section VII, we describe preliminary calculations for an experiment in which a Si cone is driven by a plane wave at its base and radiation is measured exiting from a small hole at its tip. The plane wave couples to multiple cone modes and the exiting fundamental mode (TE10) couples to numerous modes in air as well as reflected modes in the cone; so these are complicated mode-matching problems that must be solved numerically. We find that roughly half the incident power in the plane wave couples to the fundamental mode, and, at the tip of the cone, it is nearly totally reflected if the hole diameter is half the wavelength in bulk Si; facts that are used in our design study in Section VII.

VI. Electromagnetic modes of a conducting cone

Electric and magnetic fields are assumed to have the time dependence $\mathbf{E}=\mathbf{E}e^{-i\omega t}$, $H=\mathbf{H}e^{-i\omega t}$.

The conical geometry dictates use of spherical polar coordinates (r,θ,ϕ), with the conducting boundary at $\theta=\theta_c$, the cone half-angle.

The spatial fields may be expressed as linear combinations of transverse electric modes TE (E_r=0) and transverse magnetic modes TM (H_r=0). The field with the non-vanishing longitudinal component is denoted $\psi \equiv$ {**H** for TE, **E** for TM}, and that component obeys the scalar wave equation:

$$(1/r^2)[(r^2\psi_r)_{,rr} + (1/\sin\theta)(\sin\theta\psi_{r,\theta})_{,\theta}+(1/\sin\theta^2)\psi_{r,\phi\phi}] + k^2\psi_r = 0 \quad (1a)$$

$$k^2 = \varepsilon\mu\,\omega^2 = (2\pi/\lambda)^2 \quad (1b)$$

Other field components can be found from ψ_r [17].

Separation of variables $\psi_r \propto (X(x)/x^2)\,\Theta(\theta)\,\Phi(\phi)$, with $x \equiv kr$ yields the results that X, Θ, Φ are proportional to Hankel, Legendre, and trigonometric functions, respectively, as described below. The resulting solution for no charge or current sources and homogeneous material (ε, μ constant) is

TE:
$$E_r = 0 \quad (2a)$$
$$E_\theta = ZH\cos(m\phi)\; X^{\pm}_{\nu}(x)/x \;\; \Theta_l^m(\theta)\,(m/\sin\theta) \quad (2b)$$
$$E_\phi = ZH\sin(-m\phi)\; X^{\pm}_{\nu}(x)/x \;\; \Theta_l^m(\theta)_{,\theta} \quad (2c)$$
$$H_r = -iH\sin(m\phi)\; X^{\pm}_{\nu}(x)/x^2 \;\; \Theta_l^m(\theta)\,l(l+1) \quad (2d)$$
$$H_\theta = -iH\sin(m\phi)\; X^{\pm}_{\nu}(x)_{,x}/x \;\; \Theta_l^m(\theta)_{,\theta} \quad (2e)$$
$$H_\phi = -iH\cos(m\phi)\; X^{\pm}_{\nu}(x)_{,x}/x \;\; \Theta_l^m(\theta)\,(m/\sin\theta) \quad (2f)$$

TM:
$$H_r = 0 \quad (3a)$$
$$H_\theta = H\sin(m\phi)\; X^{\pm}_{\nu}(x)/x \;\; \Theta_l^m(\theta)\,(m/\sin\theta) \quad (3b)$$
$$H_\phi = H\cos(m\phi)\; X^{\pm}_{\nu}(x)/x \;\; \Theta_l^m(\theta)_{,\theta} \quad (3c)$$
$$E_r = -iZH\cos(m\phi)\; X^{\pm}_{\nu}(x)/x^2 \;\; \Theta_l^m(\theta)\,l(l+1) \quad (3d)$$
$$E_\theta = -iZH\cos(m\phi)\; X^{\pm}_{\nu}(x)_{,x}/x\;\Theta_l^m(\theta)_{,\theta} \quad (3e)$$
$$E_\phi = -iZH\sin(-m\phi)\; X^{\pm}_{\nu}(x)_{,x}/x\;\Theta_l^m(\theta)\,(m/\sin\theta) \quad (3f)$$

Here the field components are coefficients of unit vectors in the coordinate directions, {$\mathbf{e_r}$, $\mathbf{e_\theta}$, $\mathbf{e_\phi}$}, e.g. $\mathbf{E} = E_r\mathbf{e_r} + E_\theta\mathbf{e_\theta} + E_\phi\mathbf{e_\phi}$ (rather than coefficients of coordinate displacements). $Z=(\mu/\varepsilon)^{1/2}$ is the material impedance.

For propagating waves X is proportional to Hankel functions:

$$X^{\pm}_{\nu}(x) = (\tfrac{1}{2}\pi x)^{1/2}\,[J_\nu(x) \pm iY_\nu(x)] \;\rightarrow_{\text{large } x}\; \exp[\,\pm i\,(x - \nu\pi/2 - \pi/4)\,] \quad (4)$$

+ for outward propagation, – for inward propagation, with Bessel functions J and Y [18].

$\Theta_\ell^m(\theta)$ is the associated Legendre function, which we scaled to give a magnitude near unity:

$$\Theta_\ell^m(\theta) = P_\ell^m(\cos\theta)[\ell(\ell+1)]^{-m/2} \;\rightarrow_{\text{small }\theta}\; J_m(\nu\theta) \quad (5)$$

Equation (1) relates the indices of Θ_ℓ^m and X_ν, giving a dispersion relation,

$$\nu^2 = \ell(\ell+1) + \tfrac{1}{4} \quad (6)$$

The fields satisfy boundary conditions appropriate to a perfect conductor at the surface of the cone, $\theta=\theta_c$:

$$E_r(\theta_c) = E_\phi(\theta_c) = 0; \quad H_\theta(\theta_c) = 0 \tag{7}$$

These will be satisfied for

$$\text{TE: } \Theta_l^m(\theta_c),_\theta = 0 ; \quad \text{TM: } \Theta_l^m(\theta_c) = 0 \tag{8}$$

Modal values ℓ_{TEmn} and ℓ_{TMmn} are the n^{th} smallest values giving the zeroes (8). Corresponding modal values ν_{TEmn} and ν_{TMmn} are determined by (6).

Θ_l^m can be evaluated as a hypergeometric function [19], but, since our cones are narrow, the small-angle approximation in (5) is useful: In this approximation, ν is related to the Bessel function zeroes $J_m(j_{mn})=0$, $J`_m(j`_{mn})=0$. These values are

TE: $j`_{mn}$	n=0	n=1	n=2
m=0	3.832	7.016	10.173
m=1	1.841	5.331	8.536
m=2	3.054	6.706	9.969

TM: j_{mn}	n=0	n=1	n=2
m=0	2.405	5.520	8.654
m=1	3.832	7.016	10.173
m=2	5.136	8.417	11.620

Thus, approximate values for ν for the nodes are

$$\text{TE: } \nu_{TEmn} \approx j`_{mn}/\theta_c ; \qquad \text{TM: } \nu_{TMmn} \approx j_{mn}/\theta_c \tag{9}$$

The value of ν determines the longitudinal profile of the fields $X_\nu(x)$. Penetration within the cone is better for smaller ν. For illumination with linear polarization, only the dipole modes (m=1) will be excited. The two dipole modes with best penetration have $\nu_{TE10} \approx 1.841/\theta_0$ and $\nu_{TM10} \approx 3.832/\theta_0$. This difference implies the TM mode does not couple as well to the detector. Additionally, it is not excited as well by the incident radiation. Therefore, we need only consider the behavior of the TE10 mode.

VII.A. Conceptual detector design and approximate performance

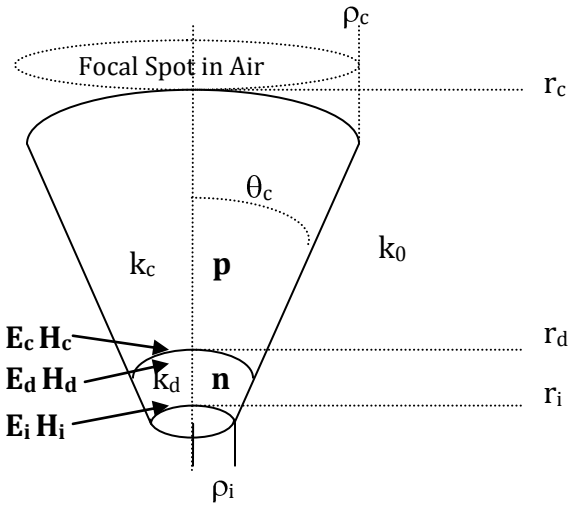

Figure 10. Photodiode geometry with two HdCdTe semiconducting layers. The p-type semiconductor is made transparent and comprises most of the cone. The n-type is absorbing and is situated to allow maximum absorption with minimum volume.

Figure 10 shows the notional detector. It consists of an outer, transparent region and an inner photo-collecting region, doped to form an n-p diode. The transparency of the material is determined by the relative amount of cadmium: a higher concentration leads to a higher band-gap energy, and little absorption at longer wavelengths. The cone surface is coated with a highly conducting metal, which must be absent around the n-p junction.

This design supposes that a diode junction can be formed between two $Hg_{1-x}Cd_xTe$ species with somewhat different Cd concentrations x. Alternatively, the transparent part of the cone could be made of silicon, which has a similar index of refraction and would give similar performance. A more conventional HCT photodiode configuration [20] could then be used, with a thin, highly doped p-type layer toward the apex of the cone.

The base radius ρ_c is appropriate to the size of the diffraction-limited focal spot of the external optical system, $\sim 4/k_0$, with k_0 the wave number in air. (This is the dimension used in the experiment described in Section IX.) The corresponding axial radius r_c is the distance from the cone apex, and depends on the half-angle θ_c; a weak parameter in this discussion.

The incident radiation is assumed to be dipole (m=1) with similar angular dependences for **E** and **H**; thus, equal powers when decomposed into TE and TM modes in spherical coordinates. We shall see that the TE10 mode is readily excited and propagates into the cone, carrying roughly half the power of the incident radiation to the detector. The TM modes contribute little.

The junction between the body of the cone, with wave number $k_c = n_c\, k_0$ (n_c real), and the detector, with $k_d = n_d\, k_0$ (n_d complex), is at axial radius r_d. The approximate radius of the r_d surface is $\rho_d \sim 2/k_c$ for good power transmission τ_d into the detector.

The inner axial radius of the detector is r_i, which is sufficiently small that there is nearly perfect reflection, even if this surface is open to air. The axial size of the detector, $r_d - r_i$, must be large enough to absorb the radiation. A surprisingly small size

$$(r_d - r_i) \sim 0.3/\mathrm{Im}(k_d) \tag{10}$$

proves adequate, probably because the cone is now small enough that the fields have departed from their asymptotic, nearly plane-wave behavior. This reduction in mean free path is another advantage of the conical geometry.

These rules-of-thumb, which will be justified presently, lead to an absorbed power somewhat less than 50% of that incident on the cone and a power-to-volume ratio

$$P/V \sim 0.1\, P_0\, (k_c)^2\, \mathrm{Im}(k_d) \tag{11}$$

By comparison, a conventional planar detector might have a radius of $\rho_c = 4/k_0$, typical of a diffraction spot, and unit optical depth (37% radiation loss vs. ~40% loss in the cone). For it

$$P/V|_0 \sim (1-e^{-1})P_0 / 16\pi k_0^2\, \mathrm{Im}(k_d) \tag{12}$$

These are in the ratio

$$(P/V) / (P/V|_0) \sim 10\, n_c^2 \sim 100 \tag{13}$$

So, there is great potential advantage in enhancing the ratio of signal to volume-dependent noise, by reducing the size of the detector in this manner.

To justify these results by a more careful treatment we evaluate the transmission of power into the detector by considering the **E** and **H** fields at r_d and r_i. These fields can be expressed as linear combinations of ingoing (–) and outgoing (+) waves of the TE10 mode. If $\mathbf{E}_c^+$,$\mathbf{E}_c^-$, $\mathbf{H}_c^+$,$\mathbf{H}_c^-$ are the modal fields for TE10 from equations (1), the total fields outside the detector at r_d are

$$\mathbf{E_c} = A_c^+ \mathbf{E}_c^+ + A_c^- \mathbf{E}_c^- \quad ; \quad \mathbf{H_c} = A_c^+ \mathbf{H}_c^+ + A_c^- \mathbf{H}_c^- \tag{14}$$

A_c^- is determined by the power flowing into the cone. A coefficient for the reflection is

$$r_c = A_c^+ / A_c^- \tag{15}$$

Considerations of average power flow using the Poynting vector show that the fraction of the power of the incident mode that flows into the detector must be

$$\tau_c = 1 - |r_c|^2 \tag{16}$$

The components of **E** and **H** tangential to the surface r_d are continuous. At r_i the tangential component of **E** vanishes due to the metal coating.

Since we consider only the single mode TE10 the angular dependences of the fields in cone and absorber will be similar. Thus, the reflection coefficient can be evaluated using modal field values at any point on the surfaces; for example, with $\theta = \phi = 0$ we have

$$r_c = \frac{-E_c^-{}_\theta\left(E_i^+{}_\theta H_d^-{}_\phi - E_i^-{}_\theta H_d^+{}_\phi\right) + H_c^-{}_\phi\left(E_i^+{}_\theta E_d^-{}_\theta - E_i^-{}_\theta E_d^+{}_\theta\right)}{E_c^+{}_\theta\left(E_i^+{}_\theta H_d^-{}_\phi - E_i^-{}_\theta H_d^+{}_\phi\right) - H_c^+{}_\phi\left(E_i^+{}_\theta E_d^-{}_\theta - E_i^-{}_\theta E_d^+{}_\theta\right)} \tag{17}$$

The field components for the ± modes at c, d, i can be found from (2). However, the reflection coefficient r_c can be determined from ratios of these components at the three positions. Therefore, the following Hankel-function substitutions in (17) can be made to simplify the calculation:

$$E^{\pm}_{\theta} \sim [J_{\nu}(kr) \pm iY_{\nu}(kr)] \qquad H^{\pm}_{\phi} \sim k[J_{\nu}`(kr) \pm iY_{\nu}`(kr)] \tag{18}$$

We have for power / volume, with 50% coupling of incident power P_0 to TE10,

$$P/V = 0.5\, P_0\, \tau_c / \{(\pi/3)\, \rho_d^2\, r_d\, [1-(r_i/r_d)^3]\} \tag{19}$$

VII.B. HgCdTe detector point designs

A $Hg_{1-x}Cd_xTe$ detector could be useful for vacuum wavelengths of 2 – 11μm, depending upon the cadmium concentration x. The optical constants measured for a typical pair of concentrations (x = 0.310, 0.226) are given in Figure 11. These give band gap energies of 0.3 and 0.2 eV, respectively, and so would produce a detector sensitive at 4-6 μm.

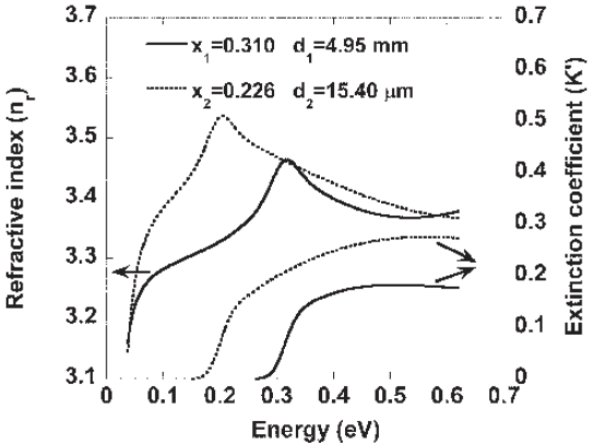

Figure 11. Measured optical constants for x in $Hg_{1-x}Cd_xTe$. From Moazzami, et al.[21]

We use this data to calculate straw-man designs. P/V is used as the figure of merit to adjust the design parameters ρ_d, ρ_i, θ_c. This optimization is made separately at the extreme wavelengths ~4 and ~6 μm. Results are shown in Table I. The optimized P/V is virtually independent of the cone angle θ_c (small angles are very slightly preferred), although optimum values of ρ_d and ρ_i depend somewhat on the choice of θ_c: Values in the table use θ_c=0.165 rad only because this is a useful baseline in the experimental baseline. The table compares P/V estimated for the detector with that of a conventional design with unit optical depth, as in eq. (12). Our estimate of a 2 orders-of-magnitude advantage for the cone design is borne out by these calculations.

Table I. Optimized design parameters for detectors at two wavelengths, for the $Hg_{1-x}Cd_xTe$ species of Figure 11

Vacuum wavelength	λ_0 =4.6 μ	λ_0 =6 μ
Cone index n_c (x=0.310)	3.384	3.333
Absorber index n_d (x=0.226)	3.483 + 0.178i	3.535 + 0.098i
Base diameter $2\rho_c = (4/\pi)\lambda_0$	5.8 μ	7.6 μ
Absorber dia. $2\rho_d \approx (2/\pi)\lambda_c$	0.93 μ	1.20 μ
Inner diameter $2\rho_i \approx \lambda_d/2$	0.56 μ	0.83μ
Cone half-angle θ_c (assumed)*	0.165 rad	0.165 rad
Detector volume	0.39 μ^3	0.88 μ^3
Power into TE10 (assumed)	0.5 P_0	0.5 P_0
Transmission into detector τ_d	0.70	0.58
P/V	0.90 P_0 μ^{-3}	0.33 P_0 μ^{-3}
Ref. Vol. $\pi\rho_c^2/\mathrm{Im}(k_d)$	110 μ^3	426 μ^3
Ref. P/V	0.0057P_0 μ^{-3}	0.0015 P_0 μ^{-3}
(P/V) / (Ref. P/V)	158	222

*****The optimized value of P/V is insensitive to θ_c (see text.)

P/V estimates for wavelengths between 4 and 6.5 μm are given in Figure 12 for the 6 μm design and for a series of redesigns to the specific wavelength (aperture size appropriate to diffraction spot, maximum P/V for the cone, unit optical depth for the reference design, etc.). The corresponding ratio of P/V for the cone to the reference is shown in Figure 13.

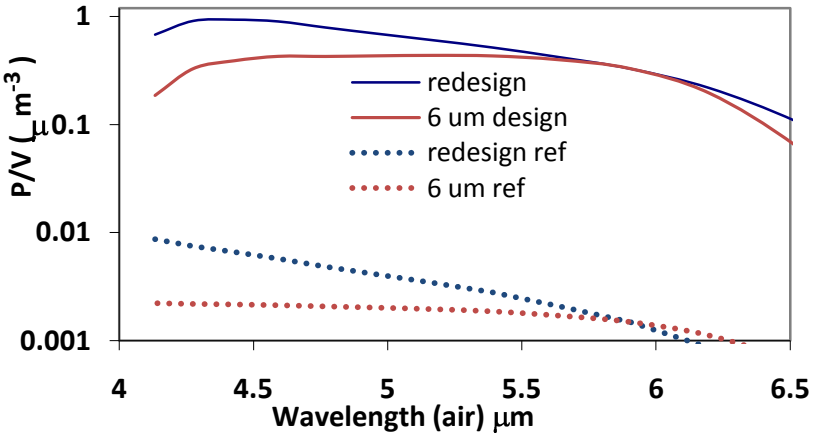

Figure 12. Power / Volume for the cone and reference detectors for the 6μm design and redesigns of the two detectors to the specific wavelengths.

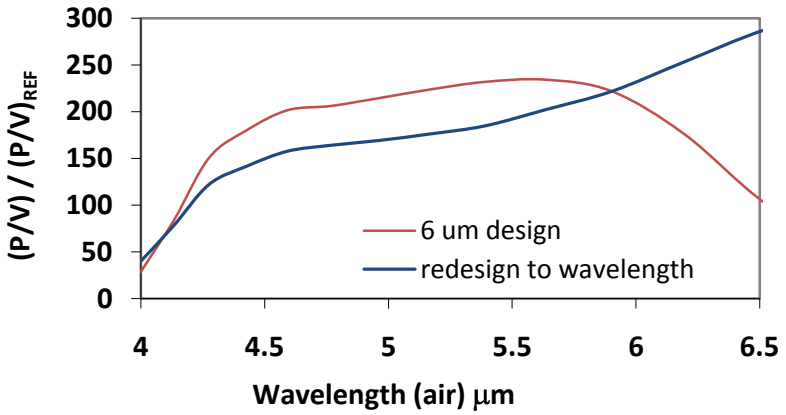

Figure 13. Ratio of the Power / Volume figure of merit for the cone to the reference design, as in Figure 12.

The 6 μm design performs consistently at shorter wavelengths, down to ~4 μm, where absorption in the (transparent) n-type HCT becomes noticeable. At longer wavelengths, the (absorbing) p-type material loses its opacity and the longer wavelengths do not propagate well into the relatively small-diameter absorber. The power-to-volume ratio is greater than 200 times that of the reference detector over this range. Thus, even though the long-wavelength point design exploits wavelength-dependent properties of propagation deep in the cone, it is useful over the entire wavelength range appropriate to the material opacities. (The same is not true of the 4.6 μm point design at the short-wavelength limit: longer wavelengths will be reflected at the absorber.)

Redesign gives greater advantage to the reference design, since its diameter is then proportional to wavelength, whereas the diameter of the absorber in the cone concept is more constrained. Hence, the performance ratio is typically smaller over the wavelength range, typically about 150. This still indicates an enormous potential advantage for the cone concept.

VIII. Measuring transmission in a conducting cone

We are preparing to perform an experiment in which a conducting Si cone is driven by a plane wave in bulk Si and the power flowing into a probe above a hole at the cone tip is measured. A main purpose of the experiment is to validate a theoretical treatment such as this, since many aspects of the problem are complicated. There could also be practical utility for a system that can create a field in air of dimensions smaller than a diffraction-limited focus. (Here, down to half the local wavelength in Si.)

The wavelength in air of the driving radiation is $\lambda_0 = 1.55$ μm. The radiation strikes a Si substrate at normal incidence. The index of refraction of Si at the laser wavelength is $n_c = 3.481$. The "incident power transmission" is $\tau_i = 4\, n_c /(1+n_c)^2 = 0.89$. Thus, little power is lost in reflection at the air/Si interface.

The radiation continues as a plane wave until it strikes the base of a clad Si cone of 2.05 μ diameter. This diameter is the diffraction spot size in air for a f=2.05μ/1.55μ=1.33 optical system, a reasonable f-number, which we use for other wavelengths.

At the base of the cone the plane-wave fields must be expanded in cone modes to determine the coefficient of the fundamental mode TE10. This is the topic of IV.A. Our calculations show significant power associated with this mode. They are consistent with the heuristic assumptions that half the power is initially in TE and nearly all that in TE10. The power transmission into the cone cuts off if the base diameter is half the local wavelength, and is 35% for a full wavelength.

There is no hindrance to the propagation of modes in the cone. However, at the hole at the tip of the cone there is a severe impedance mismatch for all higher modes, and they are nearly perfectly reflected. To calculate the transmission of TE10 through the hole, very many modes must be matched. The transmission cuts off for a hole diameter of a half wavelength, but is only 7.5% for a full wavelength, much smaller than for the inward transmission above. The difference is likely that the interface is Si – Si going in, but Si – Air coming out.

The final set of calculations, remaining to be made, concerns the coupling of the field from the hole (expressible as a Bessel series) to the measurement probe, which has an end of approximately 200μ dia., with a projecting fiber of about 4μ dia. This calculation will use much the same methodology as for the transmission from the hole.

VIII.A. Propagation into the cone

The fields of the plane wave in the substrate are

$$\mathbf{H} = H_S\, e^{-ikr\cos\theta}\,[\,\mathbf{e}_y = \cos\phi\mathbf{e}_\phi + \sin\phi(\cos\theta\mathbf{e}_\theta + \sin\theta\mathbf{e}_r)] \tag{20a}$$

$$\mathbf{E} = -ZH_S\, e^{-ikr\cos\theta}\,[\,\mathbf{e}_x = -\sin\phi\mathbf{e}_\phi + \cos\phi(\cos\theta\mathbf{e}_\theta + \sin\theta\mathbf{e}_r)] \tag{20b}$$

On the surface of the large end of the cone $x = x_c$ these fields match the ingoing m=1 cone modes. The TE and TM modes match H_r and E_r, respectively. Thus we seek mode amplitudes H_{TE1n} and H_{TM1n} such that

$$H_r = \Sigma_n\, -i\, H_{TE1n}\, X^-_\nu(x)/x^2\, \Theta^1_\ell(\theta)\, \ell(\ell+1)\sin\phi \quad = H_S\, e^{-ix\cos\theta}\sin\theta\sin\phi \tag{21a}$$

$$E_r = \Sigma_n\, -iZ\, H_{TM1n}\, X^-_\nu(x)/x^2\, \Theta^1_\ell(\theta)\, \ell(\ell+1)\cos\phi = -Z\, H_S\, e^{-ix\cos\theta}\sin\theta\cos\phi \tag{21b}$$

In the above, ν and ℓ have the values appropriate to the mode TE1n or TM1n. This scheme neglects reflections due to impedance mismatch and is only appropriate if the base diameter of the cone is larger than about half the local wavelength.

The quantities in (21a) and (21b) are evaluated for a number of θ and the resulting two systems of linear equations solved by least squares. We found that matching E_r and H_r in this manner gave reasonable agreement for the other field components. Alternatively, since Q is approximated by a Bessel function, the (approximate) Bessel series in (21) can be inverted. This would provide a relatively simple check of the mode match.

The ratio of the power associated with a mode on x_c with that of the plane wave is the "input coupling transmission" τ_{in}. This measure neglects the interaction between TM and TE modes, which are not orthogonal. However, TE10 couples much better to the incident plane wave and its transmission across boundaries deep in the cone is also much better than for other modes. Therefore, all other modes may be ignored.

τ_{in} is 45% for TE10 with baseline dimensions, $D/\lambda_{Si} = 4.5$, and is insensitive to cone angle. τ_{in} is much smaller for TM10, about 0.8% for baseline dimensions, and increases with cone half-angle. The transmission falls for a base diameter less than the local wavelength in Si, as in Figure 14. Note that these results are practically independent of cone angle.

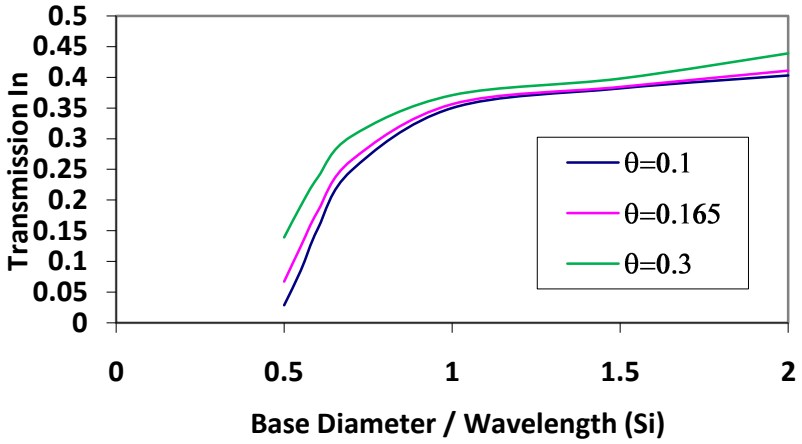

Figure 14. Transmission as a function of base diameter/wavelength for three cone angles

VIII. B. Propagation out of the cone

Suppose the cone is truncated by a horizontal cut $x=x_i$ at a small diameter. Since this is not a not a (spherical) surface of constant phase for the cone modes, their orthogonality is broken and the incident TE10 couples not only to reflected TE10 but also to all the other m=1 reflected modes, at least in principle. Furthermore, the fields of the cone modes must match on this surface to outgoing waves in vacuum. These vacuum modes can be approximated as those of a cylinder sufficiently large that their wave impedance near the cone is not affected. (We found that a cylinder diameter 8 times as large as that of the hole gave good results.) Alternatively, the vacuum field can be expressed as an integral transform.

The modes of a conducting circular cylinder are well-known [17] and need not be reproduced here. Their salient features are that the separated solution of the scalar wave equation for $\psi = \{H_z$ (TE) or E_z(TM)$\}$ in cylindrical coordinates (z, ρ, ϕ) is $\psi \propto e^{ik`z} J_m(\nu\rho) \sin(m\phi)$; the other field components can be found from $\psi$. There is a cutoff in spatial frequency $\nu$ above which the modes do not propagate ($k`$ imaginary), although they may form an important part of the near-field of the tip of a small cone.

Our methodology for this complicated match procedure is:

i) Enumerate the cone modes to be used in the match. For each mode:
ii) Find values of $H_z(\rho)$ and $E_z(\rho)$ on the aperture (in air).
iii) Find the Bessel series or Bessel transform of outgoing cylinder modes that reproduces $H_z(\rho)$ and $E_z(\rho)$.
iv) Find the difference, or mismatch, for each transverse field component between the cone mode and the Bessel expansion of cylinder modes, as a function of ρ.

v) Express the total fields a linear combination of cone modes. Determine the coefficients in this combination that minimize the overall mismatch of transverse fields. This used a linear program minimization of a least-squares error function.

We used some 20-30 cone modes and, for each, hundreds of cylinder modes, all evaluated at 100 positions ρ across the hole. Nevertheless, the computation remained quite feasible on our desktop computer. We could see graphically that all field components matched across the hole except very near the metal cylinder at its boundary.

There are two important results. The first is the transmission of the power in the incident mode to outgoing radiation in air out, which can be determined from the Poynting vector applied to the fields at the hole generated by the combination of cone modes. This transmission is shown in Figure 15. Qualitatively it is similar to Figure 14 in that there is transmission until the hole's diameter approaches half the local wavelength, but the transmission out of the hole is much smaller than that into the base for intermediate diameters. (Compare the figures for a diameter of one wavelength, for example.) Note, that this transmission considers only the radiation propagating from the cone. There is also a strong near-field, which does not propagate (the evanescent modes of the large "air cylinder").

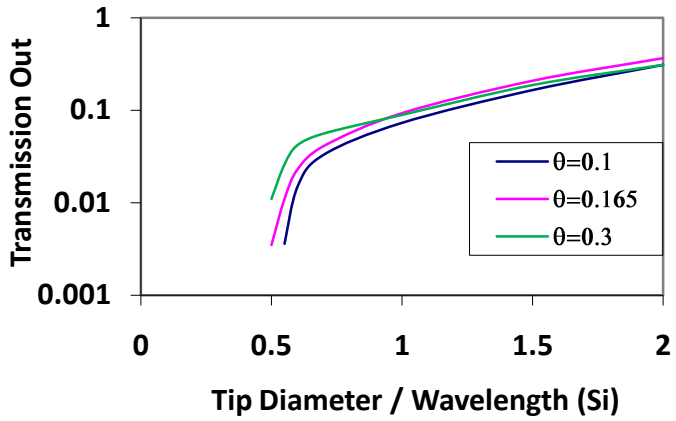

Figure 15. The fraction of radiating power from the cone, compared to that coupled to the fundamental mode. Internal reflection at the cone tip is significant, even at wavelengths short of cutoff.

The second result is that although power is flowing in air from a hole much smaller than the diffraction spot, the flux density of this radiation is not much enhanced (as it would be if the transmission were good). The average flux density is the ratio of the flowing power to the aperture area at the base and tip of the cone. The ratio of these is a simple function of the transmissions already calculated and the base and tip areas. The result is shown in Figure 16. To a fair approximation, the power radiating from a small tip aperture is proportional to its area, and the average flux density is nearly the same as that at the base of the cone. (A small enhancement in this ratio is evident for the larger cone angle, although the inaccuracy in the mode match is large compared to this possible feature.) Note that this result applies to the power radiating from the tip, not the electric fields there, which are large.

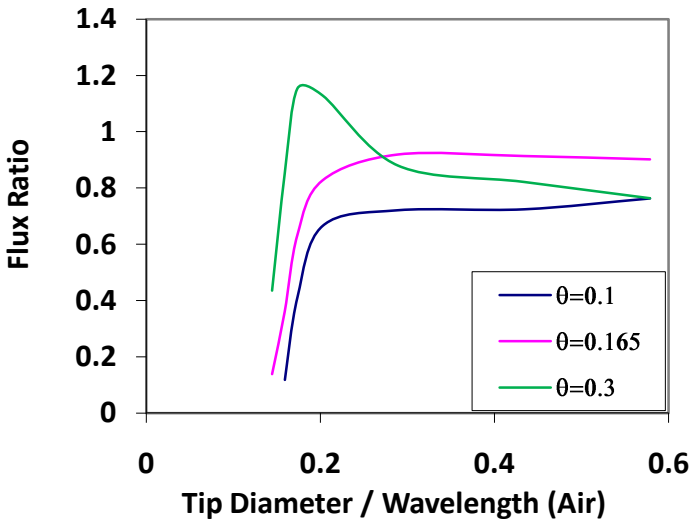

Figure 16. The ratio of power radiated to aperture area at the cone tip, compared to that at the base. Even though the tip has smaller area, transmission at the tip (Fig. 15) is such that power/aperture is not significantly enhanced. The feature for the large cone angle bears further study.

The match of fields at the cone tip determines the coefficients of the radiating modes in air. This will allow the evaluation of the power flow into the probe, for example (although there will be reflection from its surface as well). We have not yet begun exploring this further calculation. An experimental design that could measure the near-field of the cone tip would also be very useful.

IX. Fabrication and testing of light through a metal-clad cone

Superlenses of silicon were fabricated to measure light transmission through sub-wavelength structures, and to establish feasibility of the detector architecture whose performance is predicted here. These silicon cones were formed by a reactive ion etching process, and had base dimensions in the range 2-4 μm. They were designed for test light with wavelength 1.55 μm. The cone and all surrounding surfaces were sputter-coated with about 2μm of gold to prevent light transmission anywhere but through the cone. The lens aperture was created with focused ion beam milling; the diameter varied between 200 and 400 nm. A lens in cross section is shown in Figure 17, with a typical completed lens shown in Figure 18.

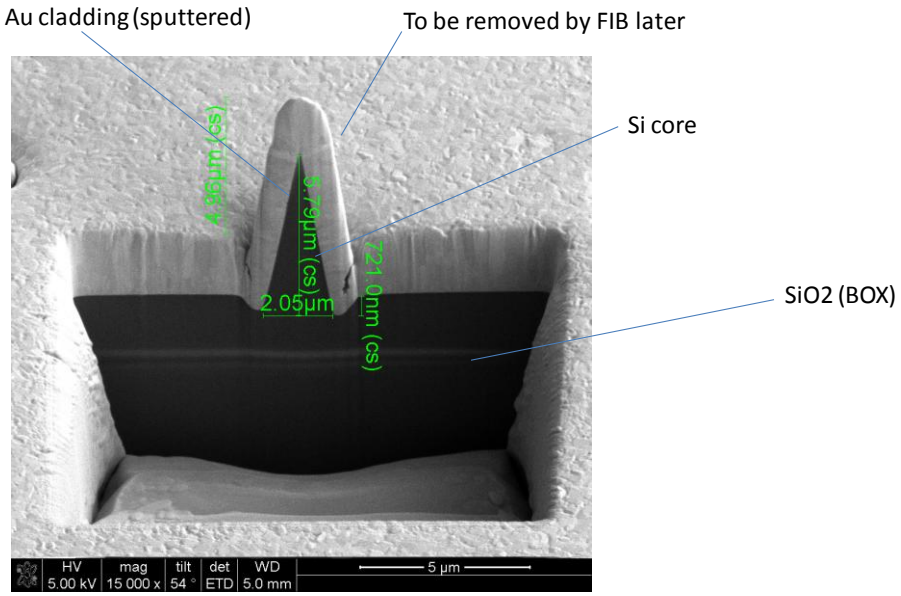

Figure 17. A silicon lens in cross section, milled by focused ion beam to view the profile of the lens and the thickness of the Au cladding.

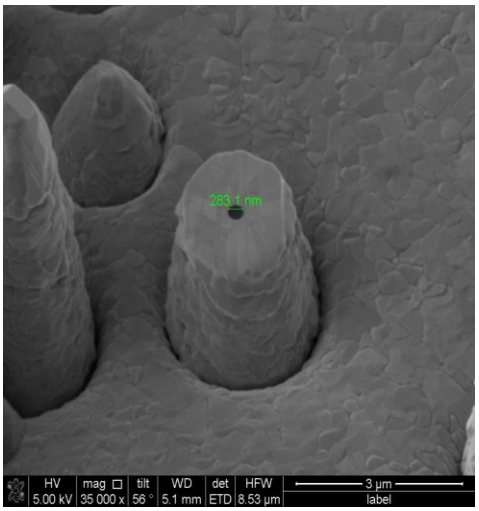

Figure 18. A scanning electron microscope image of a completed lens.

These lenses are to be tested using a near-field scanning optical microscope (NSOM), as shown in Figure 19. Here collimated with wavelength 1.55 µm diameter is directed through the base of the lens, and light passing through the lens is captured with the tip of the fiber-based NSOM. From the NSOM tip, light is transported via fiber optic to a sensitive photodetector.

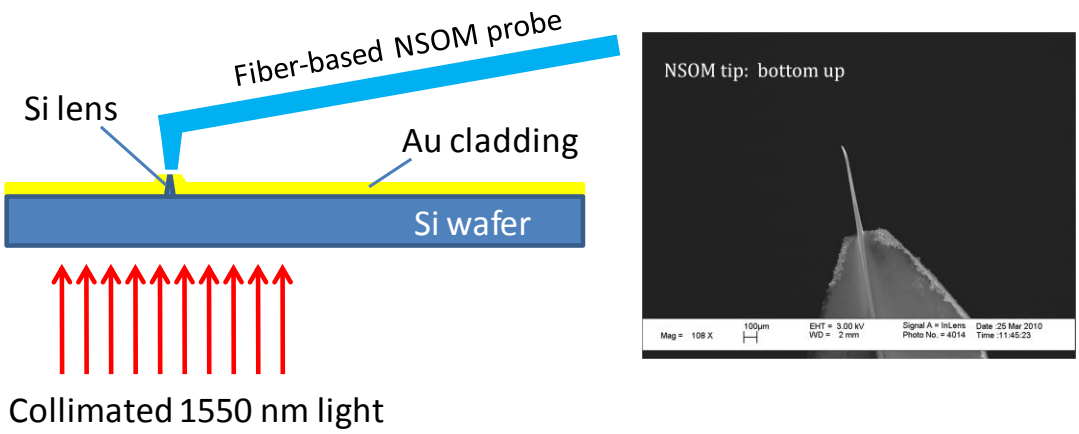

Figure 19. Experimental configuration for measuring light transmitted through a conical silicon lens.

By changing the relative position of the NSOM probe relative to the lens, the intensity profile of the transmitted light can be recorded. We anticipate that we will observe a spatially periodic intensity pattern, similar to that observed in the vicinity of an array of deep subwavelength-diameter apertures[22].

As a control, we created through-holes in the sputtered gold cladding layer near each of the lens structures under study (Figure 20). Holes with diameter 3 and 4 microns were formed, such that their diameter was much larger than the wavelength of light being measured. Just as in the case of the lens, the NSOM tip can scan over and around these holes and provide a reference for the intensity of light that is being transmitted through the silicon wafer by the collimated 1550 nm light source.

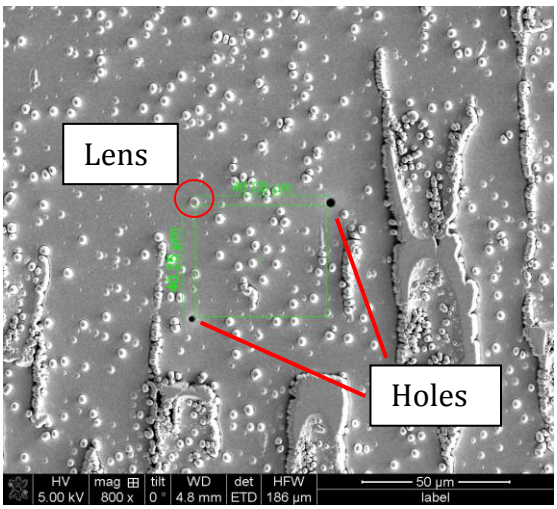

Figure 20. Top-down view of the lens and control hole structures in the silicon wafer.

We have performed preliminary transmission tests with these structures using traditional optics for focusing light onto the base of the lens. These provided a qualitative indication of light transmission through the lenses and control through-holes, and showed that our NSOM

experiments are feasible. Light can in fact be measured from lenses with deep sub-wavelength apertures. However, the more relevant NSOM experiments remain incomplete.

X. Summary – light compression for dark current reduction

An electromagnetic wave can propagate in a conducting conical cavity to very small radii. This could generate large fields in a detector inserted near the cone's tip. We find that such a detector could absorb about 40% of the power in a plane wave incident on the base of the cone, even if located where the cone's cross section is significantly smaller than the local wavelength. The power per unit volume in a HgCdTe detector in a metal-clad Si cone could be two orders of magnitude greater than that in conventional detector with the diameter of a diffraction-limited focal spot in air. Here we derived expressions for a modal expansion of the electric and magnetic fields in a conducting cone that lead to these results, and discussed a laboratory experiment to measure such fields as they exit from a small hole at the tip of the cone.

XI. Project summary

This report summarized important results of our effort to develop a new class of infrared spectrometers based on a novel broadband heterodyne design. In a model quantum well infrared photodetector (QWIP), we directly measured the beat frequency signal generated by superimposing local oscillator (LO) light and signal light in the broadband heterodyne configuration. We described how this architecture can be extended and implemented with state-of-the-art broadband light sources and detectors. We also performed calculations to determine the degree to which photodetector dark current can be reduced by suitable compression of light, since dark current scales directly with the area of the photodetector. These calculations indicate that dark current can be reduced by up to two orders of magnitude in an optimized 'superlens' structure.

Taken together, our spectrometer and dark current reduction strategies provide a promising path toward near-room temperature operation of a infrared spectrometer. Our results indicate that the broadband heterodyne approach, with integrated superlens, could lead to a near-room temperature mid-wave infrared spectrometer with performance limited only by quantum noise carried by the incoming signal. Future advancements in detector and local oscillator technology may extend the utility of this design to the long-wave infrared.

XII. References

1. H.F. Schaake, M.A.Kinch, D. Chandra, P.K. Liao, D.F. Weirauch, C.F. Wan, H.D. Shih, Proc. SPIE,7608, 760810O, 2010.
2. N.T.Gordon, C.L. Jones, D.J. Lees, C.D. Maxey, T.S. Phillips, L. Hipwood, P.C. Haynes, R. Catchpole, Proc. SPIE, 5406, 145, 2010.
3. T. Ashley, C.T.Elliott, Electr. Lett., 21(10), 451, 1985.
4. P. Klipstein, Proc. SPIE 6940, 69402U, 2008.
5. J.B.Rodriguez, E. Plis, G.Bishop, Y.D. Sharma, H. Kim, L.R. Lawson, and S. Krishna, Appl. Phys. Lett. 91, 043514, 2007.
6. C. Gmachl, D. Sivco, R. Colombelli. F. Capasso & A. Cho, Nature, 415, 883, 2002.
7. Y. Bai, S. Slivken, S.R. Darvish M. Razeghi, Proc. SPIE 7608, 76080F, 2010.
8. C.G. Stevens, N. Thomas, P. Kuzmenko, T. Alger Proc. SPIE 2266, 2, 1994.
9. H.C. Liu, et.al., IEEE Electon Device Lett., 16, 253, 1995.
10. C. Gmachl, D. Sivco, R. Colombelli. F. Capasso & A. Cho, Nature, 415, 883, 2002

11. VIGO System S.A, Product brochure.
12. Y.Yao, X Wang, J. Fan, C. Gmachl, Appl. Phys Lett., 97,081115, 2010.
13. Y. Yao, W.O. Charles, T. Tsai, J. Chen, G. Wysocki, C. F. Gmachl Appl. Phys, Lett., 96,211106, 2010.
14. R. Maulini, A Mohan, M. Giovannini J. Faist, Appl. Phys Lett. 88, 201113, 2006.
15. Y. Bai, S. Slivken, S.R. Darvish, M. Razeghi, Proc. SPIE 7608, 76080F, 2010.
16. C.L. Jones, B.E. Matthews, D.R. Purdy, N.E. Metcalfe, Semicond. Sci. Tech. 6, C110, 1991.
17. J. D. Jackson, *Classical Electrodynamics, Third Edition*, John Wiley & Sons, 1999, Ch. 8.
18. Abramowitz, M. and Stegun, I.A, *Handbook of Mathematical Functions*, Dover, 1970, Ch. 9.
19. *Ibid., p.332, 556.*
20. Graveland, O. and Gidon, S., *Electromagnetic Modeling of n-on-p HgCdTe Back-Illuminated Infrared Photodiode Response*, Journal of Electronic Materials, Vol. 37, No. 9, 2008.
21. K. Moazzami, et al., *Detailed Study of Above Bandgap Optical Absorption in HgCdTe*, Journal of Electronic Materials, Vol. 34, No. 6, 2005.
22. M. H. Chowdhury, J. M. Catchmark, J. R. Lakowicz, Appl. Phys. Lett., 91, 103118, 2007.

XII. Acknowledgements

This work summarizes results from a project, 08-ERD-016, funded by Laboratory Directed Research and Development; it was performed under the auspices of the U.S. Department of Energy by Lawrence Livermore National Laboratory under Contract DE-AC52-07NA27344.